Chinese Chemical Letters 37 (2026) 111601

Contents lists available at ScienceDirect

Chinese Chemical Letters

journal homepage: www.elsevier.com/locate/cclet

Tuning bimetallic sites in phthalocyanine-based π-d conjugated metal–organic framework cathode for wide-temperature (−20∼60 °C) potassium-organic batteries

Linqi Cheng, Jie Yu, Xupeng Zhang, Dongxue Lv, Heng-Guo Wang*

Key Laboratory of Polyoxometalate and Reticular Material Chemistry of Ministry of Education Faculty of Chemistry, Northeast Normal University, Changchun 130024, China

ARTICLE INFO

Article history:
Received 4 June 2025
Revised 8 July 2025
Accepted 17 July 2025
Available online 17 July 2025

Keywords:
π-d conjugated metal–organic frameworks
Tuning bimetallic sites
Potassium-ion batteries
Low-spin state
Ions co-storage mechanism

ABSTRACT

The orbital differentiation of transition metal ions demonstrates a critical role in modulating the structure and properties of two-dimensional π-d conjugated metal-organic frameworks (2D c-MOFs), which is possible to achieve the high-capacity and high-voltage features in rechargeable metal-ion batteries. Herein, we propose and demonstrate the strategy of coordination chemistry with different transition metal ions to construct metal phthalocyanine-based 2D c-MOFs (NiPc-8O-Cu, NiPc-8O-Ni and CuPc-8O-Cu) with different central and peripheral metal-coordination redox-active sites, which were discussed for the first time as the advanced cathode materials for potassium-ion batteries (PIBs). Benefiting from the low-spin state and the closed-shell d-orbital of central metal, NiPc-8O-Cu has higher electron/ion conductivity and stronger electron delocalization, demonstrating fascinating electrochemical performance, including a high reversible specific capacity (194 mAh/g at 0.2 A/g) and a well long-term cycling performance (over 3000 cycles at 5.0 A/g). It is worth noting that NiPc-8O-Cu can also showcase the good cycle performance at wide-temperature (−20∼60 °C). These findings provide a general guideline for the development of high-performance 2D c-MOFs as electrode materials for metal-ion batteries by engineering "inside and outside" active-site strategy.

© 2026 Published by Elsevier B.V. on behalf of Chinese Chemical Society and Institute of Materia Medica, Chinese Academy of Medical Sciences.

With the rapid consumption of lithium resource and the huge fluctuation of lithium price, the development of cost-effective and sustainable energy storage systems other than the traditional lithium-ion batteries (LIBs) is urgent [1–8]. In response, potassium-ion batteries (PIBs) are regarded as potential and efficient alternatives due to their high natural abundance, low cost and safety [9,10]. Moreover, their similar electrochemical properties with LIBs endow the compatibility with established manufacturing processes of LIBs [11–13]. However, on account of the large ionic radius of potassium ions (K^+, 1.38 Å), the traditional inorganic materials with narrow interlayer distance experience significant volumetric changes and structural collapse during the successive charging/discharging processes, leading to the suboptimal electrochemical performance [14–18]. Therefore, exploring novel electrode materials with good K^+ storage capability is crucial to develop the advanced PIBs with the extensive application prospects.

Two-dimensional π-d conjugated metal-organic frameworks (2D c-MOFs) are a distinct category of organic polymers, which have enhanced conductivity and efficient electron transfer ability due to the coordination between transition metal ions and π-conjugated organic ligands [19–24]. Besides, the extended π-d conjugated center has abundant unsaturated bonds and multivalence metal ions, which can generate additional redox-center and transfer multiple electrons/ions (Fig. 1a) [25–30]. Meanwhile, the controllable pore sizes and stable framework structures of 2D c-MOFs can also accelerate the penetration and movement of electrolyte molecules, thus promoting the redox reaction more completely [31,32]. Therefore, 2D c-MOFs have displayed the well potential for metal-ion battery systems. Nevertheless, substituting the triphenylene catecholate groups with functionalized organic ligands would enable the development of 2D c-MOFs with redox-active sites, thereby enhancing both high-capacity and high-voltage features. Based on our previous researches [33,34], phthalocyanine (Pc) and derivatives are the prototypical class of planar aromatic macrocyclic molecules with 18 π electrons (Fig. 1b), which could function as the n-doping and p-doping redox sites accompanied by the insertion/extraction of anions and cations, thus generating bipolar redox-active sites with higher working voltage [32–38]. Moreover, their high conjugated π-electron systems could result

* Corresponding author.
E-mail address: wanghg061@nenu.edu.cn (H.-G. Wang).

https://doi.org/10.1016/j.cclet.2025.111601
1001-8417/© 2026 Published by Elsevier B.V. on behalf of Chinese Chemical Society and Institute of Materia Medica, Chinese Academy of Medical Sciences.

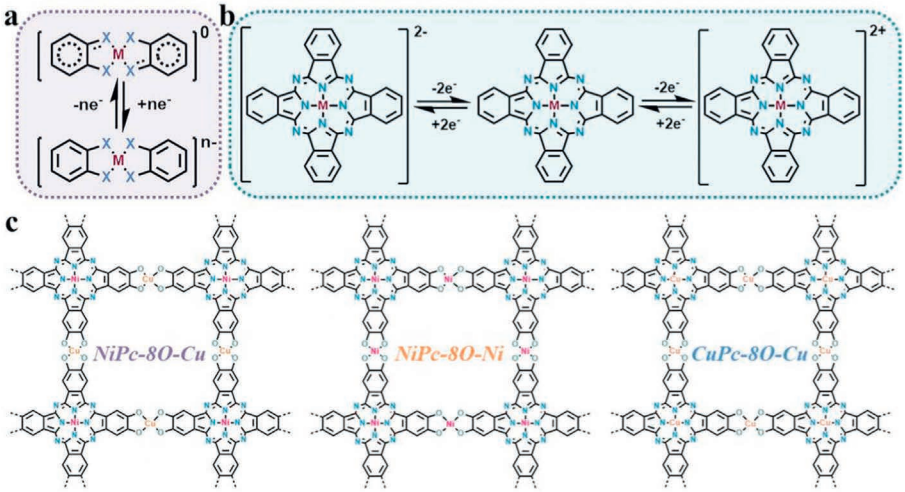


Fig. 1. (a) Schematic diagram of [MX_4] units during discharging and charging processes. (b) Two-electron oxidation (+2 charge state) and two-electron reduction (−2 charge state) of MPc units. (c) Possible chemical structures of NiPc-8O-Cu, NiPc-8O-Ni and CuPc-8O-Cu.

in fast redox kinetics and good electronic carrier ability. Noting that their central cavity consisting of four isoindole subunits could bind with various metal cations to form metalloid macrocycle complexes, thus manipulating molecular orbital recombination and electrons transfer pathway, while their variable peripheral substitution groups make them as structural units to form diverse framework structures, which makes it possible to construct Pc-based 2D c-MOFs [38,39]. Therefore, an urgent need arises to expand the practical application of Pc-based 2D c-MOFs cathodes in high-performance rechargeable metal-ion batteries through tuning bimetallic site-based redox-active sites. However, as far as we know, there are no reports about Pc-based 2D c-MOFs as the cathode materials for PIBs.

Herein, encouraged by the "inside and outside" strategy from the coordination chemistry of different transition metal ions, we designed and synthesized three Pc-based 2D c-MOFs (NiPc-8O-Cu, NiPc-8O-Ni and CuPc-8O-Cu) that constructed from (2,3,9,10,16,17,23,24-octamethoxyphthalocyaninato) M(II) (M = Cu and Ni, Fig. 1c), and first-timely used them as the cathode materials of PIBs to discuss the influence of adjusting different central and peripheral metal-coordination mode. Benefiting from the low-spin state and the closed-shell d-orbital of central metal, NiPc-8O-Cu has the internal multi-electron transfer and low spatial barriers, which is beneficial to improve the electrochemical performance. As a result, NiPc-8O-Cu delivers a reversible specific capacity of 194 mAh/g at 0.2 A/g and a well electrochemical stability with more than 3000 cycles at 5.0 A/g. Even at −20/60 °C, NiPc-8O-Cu can also showcase the good cycle characteristic, indicating the importance of structuring the bipolar 2D c-MOFs with multiple redox-active sites through the "inside and outside" strategy and coordination chemistry, confirming the extensive application of Pc-based 2D c-MOF cathodes.

To further investigate the influence of different central and peripheral metal-coordination and d-electron distribution on electrochemical performance, three types of 2D c-MOFs (NiPc-8O-Cu, NiPc-8O-Ni and CuPc-8O-Cu) were synthesized by using a simple solvothermal reaction and the synthetic details are provided Schemes S1-S5 (Supporting information). Subsequently, several characterization analyses were provided to verify the successful synthesis of NiPc-8O-Cu, NiPc-8O-Ni and CuPc-8O-Cu. Firstly, to investigate the crystallinity of three 2D c-MOFs, powder X-ray diffraction (PXRD) patterns were performed. Among them, NiPc-8O-Cu demonstrates four distinct characteristic peaks around 4.87° (100), 6.92° (110), 10.0° (200) and 21.2° (001), which infinitely close to the simulation results ($a = b = 17.91$ Å and $c = 3.40$ Å, with $\alpha = \beta = \gamma = 90°$) (Fig. 2a) [34]. Meanwhile, the broad diffraction peak around 21.2° is consistent well with the green spikes around -0.02-0.00 a.u. in the reduced density gradient (RDG) simulation, indicating the strong interlayer π–π interactions (Fig. 2b) [39]. Furthermore, PXRD patterns can also showcase the crystallinity of NiPc-8O-Ni and CuPc-8O-Cu (Fig. S1 in Supporting information), and then the RDG simulation further performs the strong π–π interactions (Fig. S2 in Supporting information) [34]. Secondly, N_2 adsorption–desorption isotherms show that the Brunauer–Emmett–Teller (BET) surface areas of three 2D c-MOFs are 310.8, 267.1 and 174.3 m^2/g and the regular dominant pore sizes are 1.42, 1.54 and 1.70 nm, respectively (Fig. 2c, Figs. S3a and S4a in Supporting information), the experimental result of NiPc-8O-Cu, NiPc-8O-Ni and CuPc-8O-Cu is consistent well with the simulation result of AA stacking structure (Fig. 2d, Figs. S3b and S4b in Supporting information). Furthermore, to further confirm their microscopic morphology, scanning electron microscopy (SEM) or transmission electron microscopy (TEM) were measured (Figs. S5 and S6 in Supporting information). Among them, NiPc-8O-Cu has the cumulate and blocky morphology, which is obviously different from NiPc-8O-Ni, CuPc-8O-Cu and NiPc-8OH. High-resolution transmission electron microscopy (HR-TEM) images of NiPc-8O-Cu can display a lattice fringe spacing of ~1.76 nm, corresponding to the [100] plane and confirming the good crystallinity (Fig. 2e). Then, the energy-dispersive spectroscopy (EDS) elemental mapping images of NiPc-8O-Cu, NiPc-8O-Ni and CuPc-8O-Cu manifest the sufficient dispersion of N/O/Ni/Cu, C/N/O/Ni and C/N/O/Cu elements (Fig. 2f, Figs. S7 and S8 in Supporting information), respectively, which agrees well with X-ray photoelectron spectroscopy (XPS) survey spectra (Figs. S9a, S10a and S11a in Supporting information). To further explore valence states of different elements, high-resolution XPS spectra were also analyzed. There are seven different peaks around 932.3/952.6 (Cu^+), 934.3/954.6 (Cu^{2+}) and 940.7/943.6/963.2 eV (satellite peak) in Cu 2p spectrum, meaning the mixed valence state of Cu ions (Fig. 2g) [31]. In the Ni 2p spectrum, the existence of Ni(II) can be confirmed by four different peaks, which are Ni $2p_{3/2}$ (855.1 eV), Ni $2p_{3/2}$ satellite (864.9 eV), Ni $2p_{1/2}$ (872.3 eV) and Ni $2p_{1/2}$ satellite (881.6 eV), respectively (Fig. S9b in Supporting information) [41]. Two different peaks belong to C=O (532.8 eV) and C–O (531.2 eV) can be discovered in the O 2p spectrum, which is attributed to the semi-quinone structure of [CuO_4] coordination center (Fig. S9c in Supporting information). Two different peaks that binding energies are 398.5 (C=N)

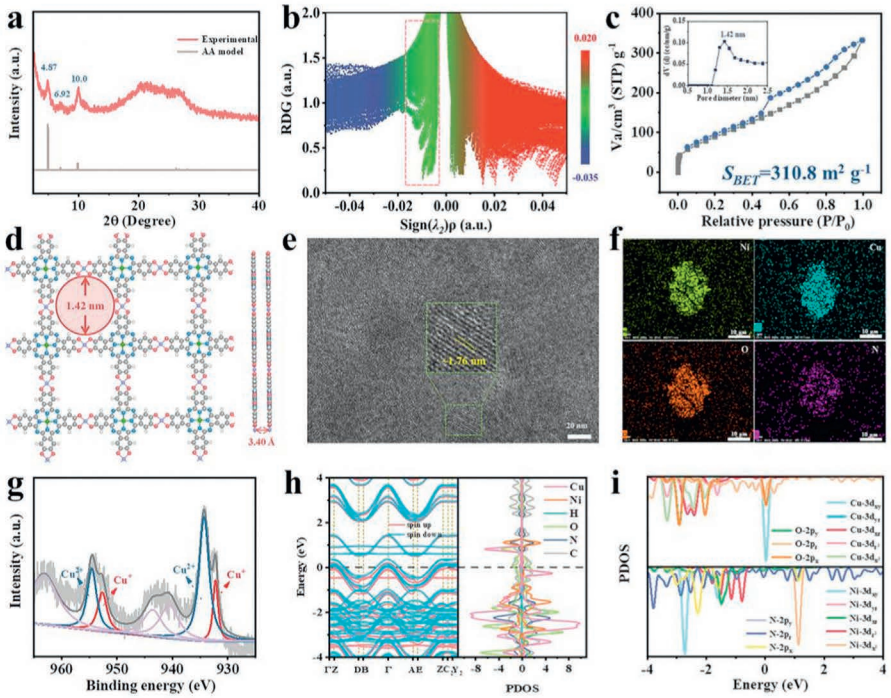


Fig. 2. (a) XRD pattern and simulation result of NiPc-8O-Cu. (b) Plots of reduced density gradient *vs.* sign(λ_2)ρ. (c) Nitrogen adsorption (square) and desorption (circular) isotherms at 77 K (inset: pore size distribution) of NiPc-8O-Cu. (d) AA model of NiPc-8O-Cu. (e) HR-TEM images of NiPc-8O-Cu. (f) Corresponding elemental mapping images of NiPc-8O-Cu. (g) Cu 2p XPS spectrum of NiPc-8O-Cu. (h, i) Electronic band structure and PDOS of NiPc-8O-Cu.

and 399.7 eV (C–N) can also be observed in the N 1s spectrum (Fig. S9d in Supporting information). Meanwhile, NiPc-8O-Ni and CuPc-8O-Cu demonstrate the similar XPS spectra with NiPc-8O-Cu, confirming the possible structures of three 2D c-MOFs (Figs. S10 and S11 in Supporting information). Furthermore, the type and composition of different functional groups were also performed by Fourier transformed infrared spectroscopy (FT-IR) spectra. Obviously, the peaks of -OH bond around 3300–3500 and 1290 cm^{-1} significantly weakened after the coordination, and then the new characteristic peak (C=O) around 1630-1660 cm^{-1} is contributed by the oxidation of the ligands (Fig. S12 in Supporting information). The existence of C–O and C=O is similar to XPS spectra, further confirming the successful coordination of Cu^{2+}/Ni^{2+} (transition metal ions) and heteroatomic groups (Pc-based conjugated organic ligands). To further understand the advantage of transition metal ions in NiPc-8O-Cu, electronic band structure and density of states were calculated. The result shows that NiPc-8O-Cu has the metallic electronic band structure due to Fermi level through ZD, BΓ, ΓA and EZ direction, which can accelerate the transport of ions and electrons (Fig. 2h). Meanwhile, the interaction of 3d (for Cu and Ni) and 2p (for O and N) can also confirm this feature (Fig. 2i) [31,42]. Moreover, thermogravimetric analysis (TGA) provides that NiPc-8O-Cu has the superior thermal stability than those of NiPc-8O-Ni, CuPc-8O-Cu, CuPc-8OH and NiPc-8OH (Figs. S13-S16 in Supporting information), and then the insolubility of three 2D c-MOFs in organic solvents and organic electrolytes was also confirmed by the dissolution phenomenon (Fig. S17 in Supporting information), which is beneficial to the electrochemical performance.

To further discuss the influence of different central and peripheral metal-coordination on electrochemical performance, coin-type half PIBs were measured at room temperature, and then several contrast experiments in different electrolytes were supplied to contrast the optimum test condition (Fig. S18 in Supporting information). Firstly, cyclic voltammetry (CV) curves of NiPc-8O-Cu were provided from 1.0 V to 3.8 V with a scan rate of 0.5 mV/s (Fig. 3a). The CV curve shows that NiPc-8O-Cu has two reduction peaks around 2.48 and 1.67 V, which can be defined as the transformation between Cu^{2+} and Cu^{+}, C=O/C=N and C–O–K/C–N–K groups, respectively. During the charging process, Cu^{+} and C–O–K/C–N–K groups gradually recover to Cu^{2+} and C=O/C=N groups around 2.85 and 2.09 V, and then another oxidation peak can be discovered at 3.24 V, which is accompanied by the combination of PF_6^- and the formation of N-PF_6 group. By contrast, the area of oxidation and reduction peaks in NiPc-8O-Ni and CuPc-8O-Cu are weaker than that of NiPc-8O-Cu, further confirming that introducing closed shell of d-orbital and multiple redox-active sites can promote the electrochemical redox reactions more completely (Fig. S19 in Supporting information). Secondly, galvanostatic charge-discharge (GCD) profiles of NiPc-8O-Cu can demonstrate a higher specific capacity (~194 mAh/g at 0.2 A/g) and a more stable capacity (~135 mAh/g at 1.0 A/g) (Figs. 3b and c) than those of NiPc-8O-Ni, CuPc-8O-Cu and NiPc-8OH (Fig. S20 in Supporting information), which is attributed to the multi-electron transfer and low spatial barriers of NiPc-8O-Cu. Meanwhile, the small organic molecules can easily dissolve in organic electrolytes, thereby NiPc-8OH showcases a poor cycling stability with a lower capacity retention. By contrast, NiPc-8O-Cu can also cycle more than 3,000 times at 5.0 A/g with a high specific capacity (101.8 mAh/g), indicating the good long-term cycling stability (Fig. 3d). Furthermore, rate performance is also a significant indicator for comparing different battery systems. Among them, NiPc-8O-Cu demonstrates higher reversible specific capacities of 154.0, 148.5, 140.2, 132.0 and 108.8 mAh/g than those of NiPc-8O-Ni (116.3, 105.2, 103.6, 98.7 and 85.0 mAh/g) and CuPc-8O-Cu (83.2, 72.6, 67.9, 65.3 and 55.7 mAh/g) at 0.4, 0.6, 0.8, 1.0 and 2.0 A/g, respectively (Fig. 3e). After cycling 100 times, the specific capacity of NiPc-8O-Cu can recover to 171.4 mAh/g at 0.4 A/g, indicating that the different central/peripheral metal-coordination and activation processes of NiPc-8O-Cu are conducive to the improvement of rate performance and electrochemical reversibility. Then, electrochemical impedance spectroscopy (EIS) was also provided to further analyze the electron/ion transfer ability. The value of semicir-

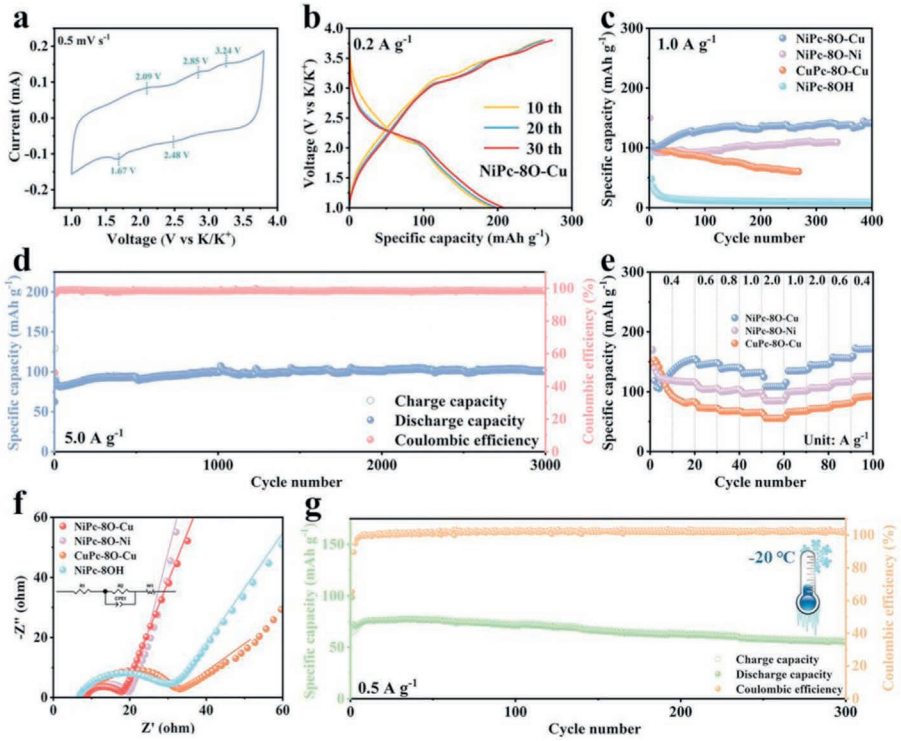


Fig. 3. (a) CV curve of NiPc-8O-Cu at 0.5 mV/s. (b) GCD profiles of NiPc-8O-Cu at 0.2 A/g. (c) Cycling stability of NiPc-8O-Cu, NiPc-8O-Ni, CuPc-8O-Cu and NiPc-8OH at 1.0 A/g. (d) Long-term cycling stability of NiPc-8O-Cu at 5.0 A/g. (e) Rate performances of NiPc-8O-Cu, NiPc-8O-Ni and CuPc-8O-Cu at different current densities. (f) Nyquist plots of NiPc-8O-Cu, NiPc-8O-Ni, CuPc-8O-Cu and NiPc-8OH. (g) Long-term cycling stability of NiPc-8O-Cu at −20 °C.

cle diameter is charge transfer resistance (R_{ct}), and then the R_{ct} value of NiPc-8O-Cu (~17.6 Ω) is significantly lower than those of NiPc-8O-Ni (~19.7 Ω), CuPc-8O-Cu (~33.1 Ω) and NiPc-8OH (~30.4 Ω), indicating that NiPc-8O-Cu has a well electrochemical behavior (Fig. 3f). To gain a deeper understanding of the reaction kinetics, CV curves at different scanning rates were provided [43]. Significantly, two pairs of reduction/oxidation peaks (recorded as R1/R2 and O1/O2) can be observed in each CV curve at 1.6, 2.0, 2.4, 2.8, 3.2 and 4.0 mV/s (Fig. S21a in Supporting information). On this basis, the charge storage mechanism of NiPc-8O-Cu is controlled by both diffusive and capacitive behaviors, which can be estimated by the calculated b values ($b_{R1} = 0.94$, $b_{R2} = 0.89$, $b_{O1} = 0.70$ and $b_{O2} = 0.87$, Fig. S21b in Supporting information). Furthermore, the contribution rate of NiPc-8O-Cu can maintain an enhancement trend (43.8 %, 46.1 %, 48.6 %, 50.8 %, 52.2 % and 54.9 %) at 1.6–4.0 mV/s, confirming the significance of capacitive behavior in the whole capacity contribution (Figs. S21c and d in Supporting information). Subsequently, to further explore the ion diffusion coefficient, galvanostatic intermittent titration technique (GITT) was tested and calculated. The result shows that the ion diffusion coefficient of NiPc-8O-Cu is mainly 10^{-9}-10^{-11} cm^2/s (Fig. S22 in Supporting information), which is higher than those of CuPc-8O-Cu (10^{-9}-10^{-12} cm^2/s) and NiPc-8O-Ni (10^{-9}-10^{-12} cm^2/s), indicating the faster kinetic process (Figs. S23 and S24 in Supporting information). Moreover, to investigate the potential and practical application of NiPc-8O-Cu, the electrochemical performance was also tested at low-temperature. At 0.5 A/g, the well capacity retention ratio of NiPc-8O-Cu is ~89 % (after 300 cycles), demonstrating that NiPc-8O-Cu has a favorable long-term cycling stability at −20 °C (Fig. 3g). By contrast, the discharge specific capacities of NiPc-8O-Ni and CuPc-8O-Cu are only 42.5 and 42.0 mAh/g at 0.5 A/g and −20 °C after cycling 100 times, and the capacity retention rates are relatively low (Fig. S25 in Supporting information). In addition, at a higher temperature (60 °C) and a larger current density (10.0 A/g), NiPc-8O-Cu can cycle more than 400 times and the specific capacity can also achieve to ~69.0 mAh/g, indicating the well cycling performance at high-temperature (Fig. S26 in Supporting information). Those consequences further confirm the advantage of different central/peripheral metal-coordination of NiPc-8O-Cu on electrochemical performances.

To further explore the storage mechanism of NiPc-8O-Cu and the change of chemical elements and functional groups during different discharging and charging processes, several characterization tests were performed and analyzed. Observing from the *ex-situ* FT-IR spectra, the intensity of characteristic peak (around 1500–1650 cm^{-1}) is significantly weakened under the continuous discharging process, indicating the reduction reaction of C=O/C=N groups (Figs. 4a and b). During the charging process, the content of PF_6^- (around 850 cm^{-1}) gradually increased, while C=O/C=N groups can recover and approach to the original state (Figs. 4b and c). Therefore, C=O (in coordination centers) and C=N (in Pc ring) are the major redox-active functional groups, which can realize the K^+ and PF_6^- co-storage mechanism in NiPc-8O-Cu. Moreover, electron paramagnetic resonance (EPR) spectra demonstrate that the EPR signal around $g = 2.15$ are contributed by Cu^{2+} in NiPc-8O-Cu (Fig. 4d). Afterwards, the EPR signal intensity gradually weakened during discharging process and significantly increased upon charging to 3.8 V, further suggesting the transformation of Cu^{2+} and Cu^+ (from $3d^9$ to $3d^{10}$) [44]. Therefore, [CuO_4] units are the important redox-active sites in NiPc-8O-Cu, which can be further proved by XPS spectra. As shown in Cu 2p XPS spectra, the intensity of Cu^{2+} gradually decreased, which is accompanied by the increased of Cu^+ at the discharging state (Fig. S27 in Supporting information). Conversely, in the following charging process, the peak intensity of Cu^+ decreased, while the peak intensity of Cu^{2+} can gradually recover to the initial state. The result is consistent well with the EPR spectra, further implying that the reversible conversion of Cu^{2+} and Cu^+ can furnish the additional redox-

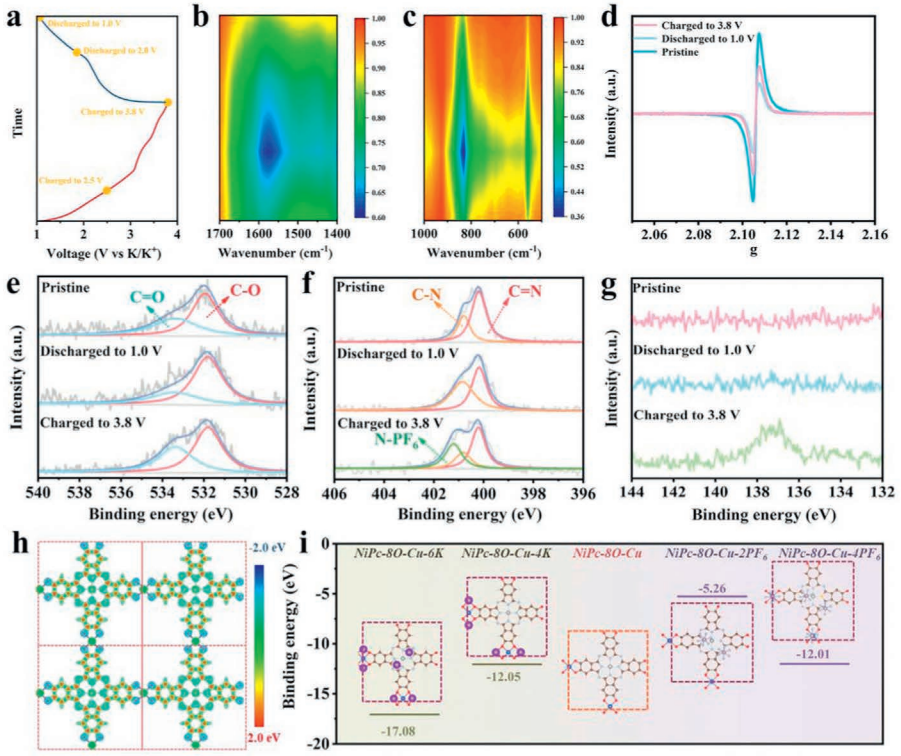


Fig. 4. (a) GCD profiles of NiPc-8O-Cu for FT-IR spectra. Contour maps of FT-IR spectra for (b) C=O, C=N and (c) PF_6^- groups. (d) EPR spectra of NiPc-8O-Cu at different discharging/charging states. XPS spectra of (e) O 1s, (f) N 1s and (g) P 2p at different discharging/charging states. (h) ESP image of NiPc-8O-Cu. (i) Binding energies for NiPc-8O-Cu repetitive unit with the most stable structure at each storage stage.

active sites. Furthermore, in the O 1s spectra, C=O/C–O groups can undergo a reversible transformation during the whole discharging and charging processes, foreboding the insertion/extraction of K^+ in C=O/C–O–K bonds (Fig. 4e). Meanwhile, N 1s XPS spectra demonstrate that C=N bond is also the main redox-active sites in NiPc-8O-Cu (Fig. 4f). To be more specific, C=N/C–N groups decreased/increased when the voltage discharged to 1.0 V, indicating the reduction of C=N and the production of C–N–K. Subsequently, a new characteristic peak around 401.2 eV can be defined as N-PF_6 group when the voltage charged to 3.8 V, suggesting that the highly conjugated π-electron system (Pc ring) can lose electrons and adsorb PF_6^-. This phenomenon is in agreement well with the variation tendency of P 2p XPS spectra with the binding energy of 136.9 eV (Fig. 4g) [40]. In addition, EDS mapping images of NiPc-8O-Cu at different charging/discharging states also demonstrate the change of K and P elements, confirming the K^+ and PF_6^- co-storage mechanism (Fig. S28 in Supporting information). To further explore the K^+ and PF_6^- co-storage mechanism of NiPc-8O-Cu, the density function theory (DFT) calculation was provided. Firstly, the molecular electrostatic potential (MESP) analysis can estimate the possible redox-active sites of NiPc-8O-Cu (Fig. 4h). On the van der Waals surface, C=N and C=O sites show the minimum value, which is easier to adsorb K^+. On the basis of experimental results and previous reports, NiPc-8O-Cu has two binding sites to adsorb PF_6^- [31,34–38]. Therefore, the binging energy values of different possible structures of NiPc-8O-Cu-2PF_6 and NiPc-8O-Cu-2K were calculated to further compare the optimal binding sites. The calculated results show that C–N bond in Pc ring has the minimum binging energy value (−2.63 eV) compared with [CuO_4] unit in coordination centers (−2.40 eV), indicating that C–N bond is more readily to combine PF_6^- than that of [CuO_4] unit (Fig. S29a in Supporting information). Thereafter, NiPc-8O-Cu-2K demonstrates the lower binding energy value on [CuO_4] unit (−3.01 eV) than that of C=N bond (−1.94 eV), foreboding the optimal structure mode (Fig. S29b in Supporting information). Because of the continuous oxidation reactions, the structure of C=N bond with 4 K^+ in the Pc ring was considered (Fig. S30 in Supporting information) [45,46]. However, the large radius of K^+ can cause an unfavorable phenomenon that the plane of C=N-4K in NiPc-8O-Cu-8K repetitive unit is distorted and the structure is unstable. Subsequently, the calculation results also demonstrate that the binding energies of NiPc-8O-Cu-2PF_6, NiPc-8O-Cu-4PF_6, NiPc-8O-Cu-4K and NiPc-8O-Cu-6K are negative, indicating the spontaneity of redox reactions. And then the binding energies gradually decreased when NiPc-8O-Cu inserts 4 K^+ (−12.05 eV), 6 K^+ (−17.08 eV), 2 PF_6^- (−5.26 eV) and 4 PF_6^- (−12.01 eV), respectively, indicating the redox reaction is sequential (Fig. 4i). Furthermore, the calculated reaction voltage is also in good agreement with the experimental tests, confirming that [CuO_4] unit can combine with 4 K^+ and 2 PF_6^-, and then Pc ring can combine with 2 K^+ and 2 PF_6^- in each NiPc-8O-Cu repetitive unit (Fig. S31 in Supporting information). To further explore the influence of different central/peripheral metal-coordination of NiPc-8O-Cu on electrochemical performances, the lowest unoccupied molecular orbital (LUMO) and highest occupied molecular orbital (HOMO) energy levels of NiPc-8O-Cu and CuPc-8O-Cu were calculated (Fig. S32 in Supporting information). Among them, NiPc-8O-Cu has the narrower LUMO–HOMO gap (E_g) of 0.88 eV than that of CuPc-8O-Cu (0.99 eV), indicating the better electrical conductivity and the superior reaction kinetics [45,46]. Therefore, NiPc-8O-Cu demonstrates the well electrochemical performance, the calculation results are consistent well with the experimental results, which highlights the importance of the highly conjugated π-electron system and multiple coordination center of MPc-based MOFs cathodes.

In summary, three 2D c-MOFs (NiPc-8O-Cu, NiPc-8O-Ni and CuPc-8O-Cu) are successfully synthesized and used as the cathode materials for PIBs. Benefitting from the unique electron rearrangement and multiple coordination centers, NiPc-8O-Cu can demon-

strate the anions and cations co-storage mechanism, manifesting the good electrochemical performance. Furthermore, different central and peripheral metal-coordination of NiPc-8O-Cu can decrease the E_g value and promote the internal electrons transfer, which can facilitate the rapid transfer and improve the electrochemical behavior. Interestingly, even at the low-temperature condition, NiPc-8O-Cu can also display a decent specific capacity, confirming the applicability and potential of NiPc-8O-Cu. Importantly, experimental and calculation results demonstrate that the anions and cations co-storage mechanism of NiPc-8O-Cu is attributed to the Pc ring (C–N/C=N) and coordination centers (C=O/C–O$^{\cdot}$ and Cu^{2+}/Cu^{+}), corresponding to the ten-electron transfer for each repetitive unit. This research exhibits a significant direction for designing high-performance 2D c-MOFs cathode with high-capacity and high-voltage features, providing a serviceable foundation for accelerating the high performance energy storage systems.

CRediT authorship contribution statement

Linqi Cheng: Writing – original draft, Methodology, Investigation. **Jie Yu:** Data curation. **Xupeng Zhang:** Software. **Dongxue Lv:** Validation, Formal analysis. **Heng-Guo Wang:** Writing – review & editing, Supervision, Funding acquisition.

Declaration of competing interest

The authors declare that they have no known competing financial interests or personal relationships that could have appeared to influence the work reported in this paper.

Acknowledgments

This work is financially supported by the National Natural Science Foundation of China (Nos. 52172186 and 22479023), and the Science & Technology Department of Jilin Province (No. YDZJ202501ZYTS301).

Supplementary materials

Supplementary material associated with this article can be found, in the online version, at doi:10.1016/j.cclet.2025.111601.

References

[1] G. Zhu, X. Tian, H.C. Tai, et al., Nature 596 (2021) 525.
[2] A.M. Desaulty, D.M. Climent, G. Lefebvre, et al., Nat. Commun. 13 (2022) 4172.
[3] X. Zhou, Q. Liu, C. Jiang, et al., Angew. Chem. Int. Ed. 59 (2020) 3802–3832.
[4] A. Masias, J. Marcicki, W.A. Paxton, ACS Energy Lett. 6 (2021) 621–630.
[5] G. Chang, Y. Zhao, L. Dong, et al., J. Mater. Chem. A 8 (2020) 4996.
[6] C. Fang, Y. Huang, W. Zhang, et al., Adv. Energy Mater. 6 (2016) 1501727.
[7] G. Zeng, B. Liu, U. Ali, et al., Appl. Catal. B: Environ. 351 (2024) 123996.
[8] X. Qiu, B. Zhang, Y. Xu, et al., Green Chem. 24 (2022) 2506.
[9] H. Zhang, X. Liu, T. Ji, et al., Chin. Chem. Lett. 37 (2026) 110790.
[10] Y. Fang, G.Y. Zhu, N.N. Zhu, et al., J. Energy Chem. 105 (2025) 312–325.
[11] Y.F. Chen, Y. Fang, N.N. Zhu, et al., Angew. Chem. Int. Ed. 64 (2025) e20242464.
[12] L. Fan, R. Ma, Q. Zhang, X. Jia, B. Lu, Angew. Chem. Int. Ed. 58 (2019) 10500–10505.
[13] L.F. Zhao, Z. Hu, W.H. Lai, et al., Adv. Energy Mater. 11 (2021) 2002704.
[14] X. Min, J. Xiao, M. Fang, et al., Energy Environ. Sci. 14 (2021) 2186.
[15] Y. Hu, W. Tang, Q. Yu, et al., Adv. Funct. Mater. 30 (2020) 2000675.
[16] Z. Chen, Y. Wu, X. Liu, et al., J. Energy Chem. 81 (2023) 462–471.
[17] H. Li, Q. Ma, Y. Yuan, et al., Adv. Funct. Mater. 34 (2024) 2301987.
[18] T. Li, Y. Wang, Q. Zhou, et al., J. Mater. Sci. Technol. 158 (2023) 86–95.
[19] M. Yang, X. Zeng, M. Xie, et al., J. Am. Chem. Soc. 10 (2024) 6753–6762.
[20] H. Xue, H. Zhu, J. Huang, Chin. Chem. Lett. 34 (2023) 107134.
[21] X. Li, J. Wang, F. Xue, et al., Angew. Chem. Int. Ed. 60 (2021) 2534–2540.
[22] P. Apostol, S.M. Gali, A. Su, et al., J. Am. Chem. Soc. 145 (2023) 24669–24677.
[23] X. Su, Z. Zhong, X. Yan, et al., J. Am. Chem. Soc. 146 (2024) 9036–9044.
[24] C. Huang, W. Sun, Y. Jin, et al., Angew. Chem. Int. Ed. 63 (2024) e202313591.
[25] M. Qi, L. Cheng, H.G. Wang, et al., Adv. Mater. 36 (2024) 2401878.
[26] L. Wang, N. Liu, X. Zhao, et al., Chem. Sci. 15 (2024) 2133–2140.
[27] K. Fan, J. Li, Y. Xu, et al., J. Am. Chem. Soc. 145 (2023) 12682–12690.
[28] M. Yang, Y. Wang, Y.F. Huang, et al., Angew. Chem. Int. Ed. 64 (2025) e202421008.
[29] L. Jiang, L. Lin, Z. Wang, et al., J. Am. Chem. Soc. 146 (2024) 22930–22936.
[30] J. Geng, Y. Ni, Z. Zhu, et al., J. Am. Chem. Soc. 145 (2023) 1564–1571.
[31] L. Cheng, M. Qi, J. Yu, et al., Angew. Chem. Int. Ed. 63 (2024) e202405239.
[32] P. Bao, L. Cheng, X. Yan, et al., Angew. Chem. Int. Ed. 63 (2024) e202405168.
[33] H.G. Wang, H. Wang, Z. Si, et al., Angew. Chem. Int. Ed. 58 (2019) 10204–10208.
[34] H.G. Wang, Q. Li, Q. Wu, et al., Adv. Energy Mater. 11 (2021) 2100381.
[35] Z. Meng, A. Aykanat, K.A. Mirica, J. Am. Chem. Soc. 141 (2019) 2046–2053.
[36] L. Cheng, L. Chen, J. Yu, et al., J. Colloid Interf. Sci. 663 (2024) 656–664.
[37] J. Zhao, M. Zhou, J. Chen, et al., Chem. Eng. J. 425 (2021) 131630.
[38] H.G. Wang, Q. Wu, L. Cheng, et al., Energy Storage Mater. 52 (2022) 495–513.
[39] H. Pan, Y. Ren, Q. Wang, et al., Coordin. Chem. Rev. 527 (2025) 216404.
[40] L. Cheng, X. Yan, J. Yu, et al., Adv. Mater. 37 (2025) 2411625.
[41] Y.H. Zhong, Y. Wang, S.Y. Zhao, et al., Adv. Funct. Mater. 34 (2024) 2316199.
[42] Y. Ni, L. Lin, Y. Shang, et al., Angew. Chem. Int. Ed. 60 (2021) 16937–16941.
[43] X. Zhou, S. Xiao, D. Yang, et al., Angew. Chem. Int. Ed. 63 (2024) e202409255.
[44] Y. Chen, Q. Zhu, K. Fan, et al., Angew. Chem. Int. Ed. 60 (2021) 18769–18776.
[45] J. Chen, H. Yin, Q. Xue, et al., Adv. Funct. Mater. 34 (2024) 2411362.
[46] X.T. Zhao, J.Z. Guo, W.L. Li, et al., Chin. Chem. Lett. 35 (2024) 108715.